

***Operando* Studies of Aerosol-Assisted Sol-Gel Catalyst Synthesis via Combined Optical Trapping and Raman Spectroscopy**

Gareth Davies¹, Justin Driver¹, Andrew Ward², Leila Negahdar^{3,4} and James McGregor^{1,4*}

¹*University of Sheffield, Department of Chemical and Biological Engineering, Mappin Street, Sheffield S1 3JD, UK*

²*Central Laser Facility, Research Complex at Harwell, Rutherford Appleton Laboratory, Didcot OX11 0FA, UK*

³*University College London, Department of Chemistry, Gordon Street, London WC1H 0AJ, UK*

⁴*UK Catalysis Hub, Research Complex at Harwell, Rutherford Appleton Laboratory, Harwell OX11 0FA, UK*

*james.mcgregor@sheffield.ac.uk

Abstract

New insights have been gained into the chemical transformations occurring in the initial stages of aerosol-assisted sol-gel (AASG) synthesis of catalysts. This has been achieved through the combined application of optical trapping and Raman spectroscopy. AASG is an emerging technology in catalyst manufacture that presents numerous advantages over conventional approaches, including the ability to access unique catalyst morphologies. However, the processes occurring during synthesis are largely inferred from bulk-phase analyses due to challenges in conducting *in situ* or *operando* measurements on moving aerosols within a flow tube. Herein, these obstacles are overcome through Raman spectroscopic interrogation of a single aerosol droplet constrained within an optical trap, which acts as direct analogue for a particle moving along a flow tube. These studies represent the first *operando* investigations of AASG synthesis. The synthesis of Ni/Al₂O₃ catalysts has been studied, with spectroscopic interrogation conducted on each component of the precursor synthesis solution, where possible, up to and including a mixture containing all components necessary for catalyst synthesis. Raman spectroscopy confirms the formation of stable self-assembled macro structures within the aerosol and provides direct insights into the reaction mechanisms. Crucially, evidence was obtained allowing alternative reaction pathways to be postulated within the confined environment of an aerosol droplet in comparison to bulk-phase syntheses. In aerosols where nickel was not present, but containing all other components, isothermal room temperature studies showed the formation of stable but unreactive droplets of ~1 μm which were proposed to comprise of micelle-type structures. Upon

heating, initial gelation transformations were seen to be effected at temperatures in excess of ~56 °C. Notably, little loss of spectral intensity corresponding to the C-H stretch (ethanol) was observed from the heated aerosol implying that evaporation is not a prerequisite for reaction. When nickel is present in the synthesis solution, reactive transformations occur at room temperature, proposed to result in a continuous Al-O-Ni-NO₃ structure; a more rapid transformation takes place at elevated temperatures. These results provide the first direct evidence of the processes occurring within aerosols during AASG and shed new light on the mechanistic understanding of this technology. This therefore facilitates the design of new synthetic approaches and hence the production of catalysts and other materials with enhanced properties.

Keywords: Optical tweezers, heterogeneous catalysis, vibrational spectroscopy, sol-gel materials synthesis, aerosol

Abbreviations and Acronyms

AASG - aerosol-assisted sol-gel

Al-iPr – aluminium isopropoxide

CMC - critical micellisation concentration

EISA - evaporation induced self-assembly

EP – aerosol comprising ethanol and P123

EPN - aerosol comprising ethanol, P123 and nitric acid

EPNA - aerosol comprising ethanol, P123, nitric acid and aluminium isopropoxide

EPNAN - aerosol comprising ethanol, P123, nitric acid, aluminium isopropoxide and nickel nitrate hexahydrate

FT-IR - Fourier-transform infrared

HEPNA – heated aerosol comprising ethanol, P123, nitric acid and aluminium isopropoxide

HEPNAN - heated aerosol comprising ethanol, P123, nitric acid, aluminium isopropoxide and nickel nitrate hexahydrate

P123 - Poly(ethylene glycol)-block-poly(propylene glycol)-block-poly(ethylene glycol)

PEO – polyethylene oxide

PPO – polypropylene oxide

WGM – whispering gallery mode

1.0 Introduction

Aerosol-assisted sol-gel (AASG) synthesis is a recently established method of synthesising nanostructured catalysts with controllable porosity and surface functionality using a continuous method which produces a low volume of waste material.¹ AASG therefore has advantages over conventional catalyst synthesis methods, however the transitions that occur during the sol-gel process within the aerosol are complex and still not completely understood. This is in part due to the challenges of conducting *in situ* or *operando* characterisation measurements in an aerosol environment.² In this work, a novel approach combining optical trapping and Raman spectroscopy is employed to directly probe these processes and hence provide insights into AASG synthesis.

AASG combines aerosol processing with sol-gel synthesis. In conventional sol-gel synthesis nanostructured materials are produced under acidic or basic conditions using templating agents (e.g. block copolymers) to control the mesophase formation of the material.³ The chemical precursors react through hydrolysis and condensation reactions to form solid compounds. Sol-gel synthesised materials have applications in adsorption, catalysis, drug delivery, and energy storage.⁴⁻⁷ While AASG is a relatively new approach to catalyst manufacturing, a number of promising metallosilicate epoxidation and acetalization catalysts have been synthesised.⁸⁻¹⁰ AASG synthesised titanium silicates were shown to be highly active for cyclohexane epoxidation giving product yields of up to 62%.¹¹ Additionally, AASG based processes have no liquid by-products, offer facile cheap collection processes with no separation, and yield high purity products with unique morphologies.

Considering the mechanism of AASG, an aerosol is created containing the same component species as in conventional sol-gel synthesis. When the aerosol is heated it is hypothesised that self-assembled micelles form.¹² Subsequently, multiple hydrolysis and condensation reactions are proposed to proceed concurrently to produce a highly branched agglomerate in the sol which ultimately becomes sufficiently cross-linked to form a gel. Both steps are either acid- or base-catalysed (Figure S1). The formation of self-assembled micelles in AASG is referred to as evaporation induced self-assembly (EISA). After this, thermal or chemical treatment is performed in order to remove templating agents and expose porosity in the catalyst.

A range of techniques have been applied to the analysis of aerosol-synthesised materials post-synthesis, characterising properties such as particle size, molecular mass, structure, composition, *etc.*¹³ However, it is highly challenging to conduct accurate spectroscopic studies of the aerosol while the synthesis reactions are taking place as the aerosol droplets travel continuously along a flow tube. A single droplet cannot therefore be tracked as a function of time. A further challenge is that chemical concentrations in a given region are typically low due to the low density of droplets. Mechanistic insights are therefore typically inferred from measurements on bulk syntheses. Raman spectroscopy of bulk solutions has been used to identify micelle formation and critical micelle concentration of surfactants which can be used in AASG.^{14,15} The onset of micelle formation and aggregation can be identified by a change in peak relative intensity, *e.g.* a change in the ratio of the asymmetric CH₃ stretching vibration to the symmetric CH₃ stretching vibration, or by a shift in peak position as surfactant concentration increase.

In the present work, these limitations are overcome through conducting Raman spectroscopic interrogation of a single aerosol droplet while it is constrained within an optical trap. Optical tweezers use focussed light to hold either liquid or solid particles in place and can be applied to particles ranging in size from 10 nm to 10s of μm .¹⁶ This is achieved by balancing the radiation pressure imparted by two focussed laser beams that are vertically (z-axis) opposed in a counter-propagating geometry. Radiation pressure arises through the transfer of momentum as photons are scattered from a surface. Here, the laser beams also have a Gaussian beam profile creating an intensity gradient to assist stability in the horizontal x and y-axes. The main physical conditions that permit trapping stability are that the levitated droplet has (i) a refractive index greater than air (ii) an element of symmetry to evenly scatter light and (iii) has low enough mass whereby the radiation pressure can offset gravitational force. Optical trapping has previously been used for other applications in conjunction with vibrational spectroscopies to provide information on the nature of multicomponent particles comprising both aqueous and organic phases.¹⁷

Monitoring a single droplet over time held in a fixed position in space provides a direct analogue for a particle instead moving through space as happens in a flow tube, with increased time corresponding to increased distance along the tube. A key development is the ability to externally heat the optical trapping cell to induce reaction. Any influence of the trapping laser on droplet heating is expected to be limited in comparison to the external heating. Boyer *et al.*

have reported minimal heating through his mechanism even at intense laser powers, while Hunt *et al.* reported only a few degrees of heating at moderate laser powers (<25 mW).^{18,19} This approach applied herein can therefore be considered an *operando* investigation of the AASG synthesis process. The reaction system of specific focus in this work is the organic transformations which occur in the initial stages of AASG synthesis of Ni/Al₂O₃, a catalyst with a wide range of current and potential future industrial applications including CO₂ utilization and biomass conversion. This will, for the first time, provide direct measurements of the reactions occurring during AASG synthesis, yielding valuable insights into this process.

2.0 Experimental

2.1 Reagents/Chemicals

The catalyst precursors employed were nickel nitrate hexahydrate (Ni(NO₃)₂·6H₂O, ≥97%) and aluminium isopropoxide (Al-iPr, ≥98%), whilst the templating agent was Pluronic[®] triblock polymer (P123, M_w ≈ 5800, PEO-PPO-PEO). The catalyst synthesis reactions were conducted in acidified solvent solution produced from mixtures of ethanol (C₂H₅OH, ≥98%) and nitric acid (HNO₃, 68%). Prior to use, ethanol was dried using molecular sieves (3 Å, Sigma-Aldrich), whereas all other chemicals were used as received. All chemicals were purchased from Sigma-Aldrich, UK.

2.2 Sol-Gel Synthesis Procedure

The synthesis procedures were adapted from previous reports describing the bulk preparation of Ni/Al₂O₃ by the EISA method.³ Under vigorous stirring a weighed quantity of P123 (1.21 g) was added to ethanol (10 mL), with the mixture then sealed and gently heated (~40 °C) to assist dissolution. Following complete dissolution of P123, a weighed quantity of Ni(NO₃)₂·6H₂O (0.49 g) was added and the solution (hereafter called “solution A”) which was then allowed to cool to room temperature. Separately, a measured quantity of Al-iPr (1.72 g) was added to a beaker, prior to addition of ethanol (10 mL). Under gentle stirring, the dropwise addition of HNO₃ (1 mL) caused gradual dissolution of Al-iPr without heating, after which the solution (hereafter “solution B”) was allowed to cool to room temperature. Following this, solution A was added rapidly to solution B under moderate stirring, consequently effecting final concentrations as follows: P123 (0.01 M); Al-iPr (0.4 M); and Ni(NO₃)₂·6H₂O (0.13 M). These quantities corresponded to a theoretical nickel loading of ~24.5 wt% in the final Ni/Al₂O₃ catalyst. All *operando* investigations were conducted on freshly mixed solutions (~1-3 days).

2.3 Bulk Analysis (*ex situ* Raman)

For bulk syntheses, freshly mixed solution was transferred to an oven and heated (~ 70 °C, 16 h) to initiate EISA, which subsequently yielded a powder composed of gel particles. A sample of this gel was retained, with the remainder transferred to a furnace for calcination (600 °C, 3 h) to afford the final Ni/Al₂O₃ catalyst. These samples were then spectroscopically analysed by *ex situ* Raman spectroscopy. Raman analysis was performed using a Renishaw inVia Raman microscope equipped with a 514 nm (green) Ar laser at a power of 12 mW. Spectra were acquired over the range 4000 – 50 cm⁻¹ employing acquisition parameters of 30 s scans and 20 accumulations.

2.4 Aerosol Analysis (*operando* Raman)

For AASG syntheses, the freshly mixed solution was transferred into a nebuliser (aerosonic, combineb model 3019) that delivered a mist of aerosol droplets into a trapping cell, the precise configuration of which is described in Section 2.5. From this aerosol, a single droplet could be trapped and lowered into the centre of an annular ceramic heater, with the applied power then increased incrementally (0-14 W) to raise the internal temperature of the cell (≤ 200 °C). The set-up has previously been described in detail by McGrory *et al.*²⁰ The heating element in the cell creates convection currents which apply viscous drag to the trapped aerosol as the flow rate increases. In the present set-up, convective flow was minimised using a baffle system. Direct temperature measurements were not possible since the positioning of thermocouples sufficiently close to the trapped droplet would disrupt the trapping beams. Instead, the cell temperature was inferred from calibration measurements performed on an empty cell, where a thermocouple could be positioned directly in the centre of the annular heater to measure the temperature over a range of powers (Figure S2). The elevated temperature in the cell initiated EISA and the incipient formation of the Ni/Al₂O₃ catalyst, which was spectroscopically analysed by *operando* Raman. Measurements were typically taken at the onset of trapping, and subsequently at intervals of 10 or 30 s over the spectral range 500 – 3100 cm⁻¹ until the droplet was lost from the optical trap. In this way, the catalyst formation could be spectroscopically interrogated under conditions representative of the AASG process.

2.5 Optical Trapping Configuration

Liquid droplets were delivered to a small trapping cell, of aluminium construction, with approximate dimensions 10 × 2 × 1 cm. Windows made from borosilicate cover slips allowed the passage of the laser beams through the cell. Droplets were generated using an ultrasonic nebuliser (aerosonic, combineb model 3019) to generate a mist which flowed into the cell

through ¼” PTFE tubing. A right angle turn in the tubing is achieved using a Portex PVC connector tube.

Droplets were trapped using counter-propagating Nd:Yag laser beams operating at 1064 nm. The typical laser beam powers required for stable trapping were 15 mW through the top objective and 10 mW through the lower objective. The objective lenses were Mitutoyo x50 NA 0.42 long working distance objectives. The asymmetric power balance was required to force the particle into the optical focus plane of the lower objective thereby allowing focused images to be acquired. The Nd:Yag beam is passed through a beam splitter (Oz Optics) to obtain two separate fibre-coupled beams. Both beams are then expanded and collimated so that they slightly overfill the back apertures of the objective lenses. Dichroic mirrors (CVI Melles Griot) reflect the laser beams but allow transmission of illumination light and the Raman signals. The LED illumination (Comar Optics) is filtered to prevent interference with the Raman signal.

Raman spectra were acquired by probing the droplet using a 514.5 nm laser. The laser was directed through the lower objective lens and focussed onto the droplet. The backscattered Raman signal was collected using the same lens and focussed into a spectrometer (Acton SP2500i and Princeton Instruments Spec 10 CCD). A 600 groves/mm grating was calibrated using spectrophotometric grade toluene as a reference. Typical laser power was 2 mW, acquisition time was 30 s, and the 514.5 nm laser was shuttered such that the droplet was only illuminated during collection of spectra.

3.0 Results and Discussion

Raman spectroscopic analysis of the bulk solutions and the catalyst obtained *via* standard sol-gel synthesis is presented in Section 3.1; while Section 3.2 presents, for the first time, the corresponding data for the initial stages of the AASG synthesis at isothermal conditions. The influence of heating is then examined in Section 3.3. Finally, Section 3.4 discusses mechanistic insights gained from these studies.

3.1 Bulk solutions

Conventional, *i.e.* non-aerosol, synthesis of Ni/Al₂O₃ *via* a sol-gel route was initially conducted in order to compare the bulk solutions to the aerosol. Raman spectroscopy characterisation of each stage of the synthesis procedure was conducted, namely: individual components; precursor sol-gel (EISA); and the final solid catalyst. The spectrum obtained for bulk ethanol

is shown in Figure 1 and this is compared to the subsequent stages of catalyst synthesis in Figure 2. The assignment of the peaks identified is shown in Table 1.

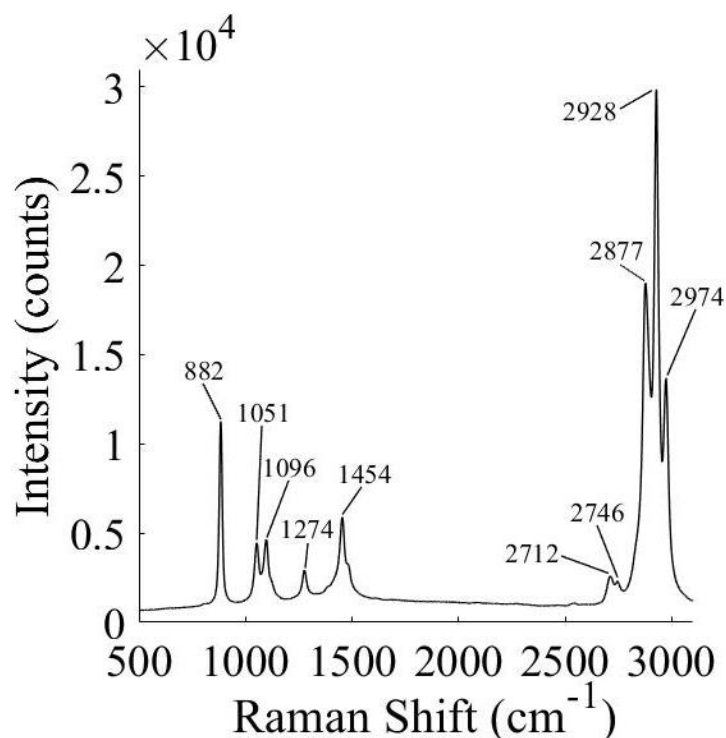


Figure 1: Raman spectra for bulk ethanol (600 groove, centred at 1900 cm^{-1} , 10 secs, 2 mW).

When comparing bulk ethanol spectral intensities to the sol precursor under identical conditions a clear decrease in peak intensity is observed indicating the reduced concentration of ethanol. There are no additional peaks present indicating that no reaction has yet taken place. The EISA sample however shows a clear increase in peak intensity of the 1048 cm^{-1} vibration, indicative of the $-\text{NO}_3^-$ symmetric stretch. This increase is ascribed to the increase in relative concentration of the nitrate component due to evaporation of ethanol during EISA. Raman bands present for the final calcined Ni/ Al_2O_3 are of only very low intensity compared to ethanol, as well as compared to the sol and gel (EISA) phases, consistent with previous literature.²¹

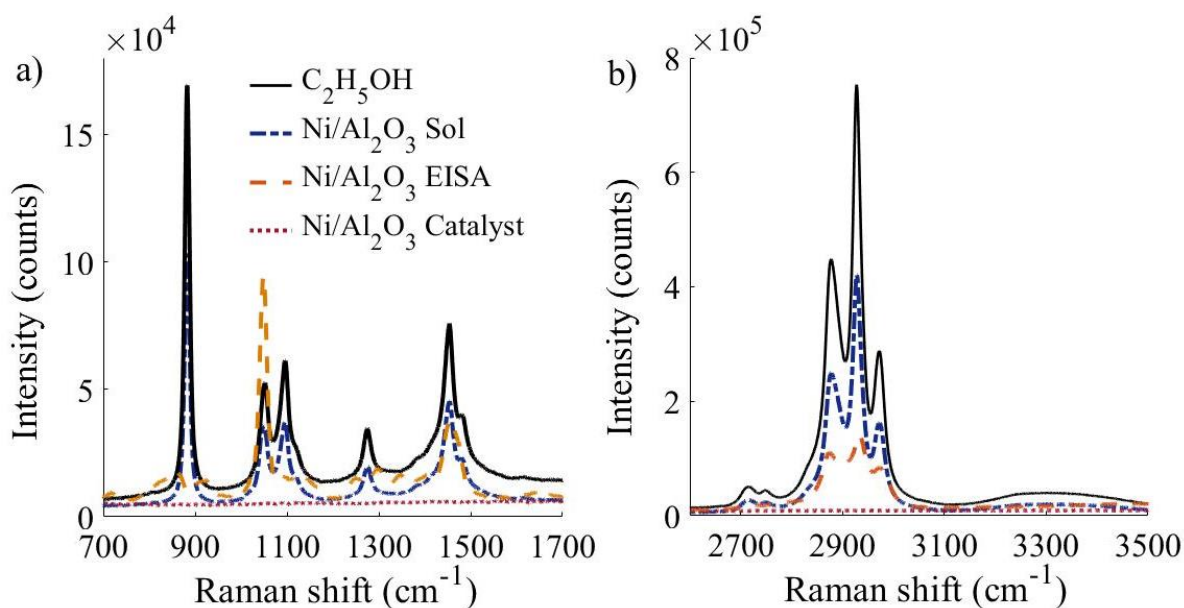


Figure 2: Raman spectra for ethanol and for Ni/Al₂O₃ sol, gel (EISA), and dried catalyst between: (a) 700-1700 cm⁻¹; and (b) 2600-3500 cm⁻¹ acquired using Renishaw inVia Raman microscope 514 nm (green), Ar laser, 12 mW.

Table 1: Bands identified in Raman spectra at different stages of Ni/Al₂O₃ synthesis. Band assignment is based on previous studies.²²⁻²⁵

$\Delta\nu$ (cm ⁻¹)	Raman band assignment	$\Delta\nu$ (cm ⁻¹)	Raman band assignment
1048	-NO ₃ ⁻ symmetric stretch	~2705	C ₂ H ₅ OH combinational frequencies
1051	C-O symmetric stretch	2744	C ₂ H ₅ OH combinational frequencies
1096	C-O asymmetric stretch	2877	CH ₂ asymmetric stretch
1274	CH ₂ torsion-rotation	2928	CH ₃ symmetric stretch
1454	CH ₃ and CH ₂ bend	2974	CH ₃ asymmetric stretch

3.2 Isothermal Aerosols

In order to determine the influence of each component upon the reactions taking place, spectroscopic interrogation was performed on each component individually, where possible, and on their mixtures up to and including that containing all components required for the AASG synthesis of Ni/Al₂O₃. The composition of the aerosols studied is summarised in Table 2; the aerosols are denoted as: EP (ethanol, P123); EPN (as EP with the addition of HNO₃); EPNA (as EPN with the addition of Al-iPr); and EPNAN (as EPNA with the addition of

Ni(NO₃)₂·6H₂O). Studies were first conducted at room temperature in order to provide a stable environment in which to study the stability of the droplets and the initial stages of gelation.

Table 2: Composition of the droplets trapped and investigated with Raman spectroscopy. Water (H₂O) is not added as a separate component but is present in nitric acid (HNO₃) and nickel nitrate hexahydrate (Ni(NO₃)₂·6H₂O) solutions. H₂O (≤2%) present in ethanol is neglected. EP (ethanol, pluronic P123), EPN (ethanol, pluronic P123, nitric acid), EPNA (ethanol, pluronic P123, nitric acid, aluminium alkoxide), EPNAN (ethanol, pluronic P123, nitric acid, aluminium alkoxide, nickel nitrate).

Reference	Component					
	Ethanol (C ₂ H ₅ OH)	Water (H ₂ O)	Triblock Pluronic (P123)	Nitric Acid (HNO ₃)	Aluminium Isopropoxide (Al-iPr)	Nickel Nitrate (Ni(NO ₃) ₂)
EP	✓		✓			
EPN	✓	✓	✓	✓		
EPNA	✓	✓	✓	✓	✓	
EPNAN	✓	✓	✓	✓	✓	✓

The presence of whispering gallery modes (WGMs) was observed in all Raman spectra for the trapped droplets, indicating sphere formation (Figure S3).²⁶ WGMs occur in the optical cavity formed by the spherical droplets as described by Mie scattering theory.²⁷ The resonance positions are dependent on droplet size and refractive index. WGMs were digitally filtered during data processing using Spectragryph (<http://spectroscopy.ninja>) adaptive baseline removal (25% coarseness) in order to aid spectral analysis. The existence of WGMs allows for the size and refractive index of the trapped particle to be estimated through Mie scattering analysis; this is explored further in Section 3.2.3.²⁸

It is notable that the H₂O content in each system is sufficiently low that Raman spectral bands associated with H₂O are not observed in the Raman spectra of the trapped aerosols over the spectral range investigated. Previous studies have shown that in bulk ethanol/water mixtures the O-H bending vibration (~1630 cm⁻¹) is of low intensity at water concentrations below ~60% v/v.²² In the present work, the water content (v/v%) of EP, EPN, EPNA, EPNAN are estimated at 2%, 3.4%, 3.2%, and 3.9% respectively based on the concentrations of the precursor solutions. Note that the strength and wavenumber of Raman vibrations associated with water may be influenced by disruptions to the mesoscale hydrogen-bonding network through interaction with other components present in solution.^{22,29}

3.2.1 Transformations in Metal-Free Droplets

Raman spectra for EP and EPN are shown in Figure 3. Characteristic Raman peaks for ethanol, *i.e.*, CH₃ and CH₂ bending vibrations at 1454 cm⁻¹ and C-H stretching vibrations at 2877, 2928 and 2974 cm⁻¹ (*cf.* Figure 1), are clearly visible and dominate the spectra of both aerosols. The evaporation of ethanol from the droplets is characterised by the reduction in intensity between the initial and final scans (Figure 3).

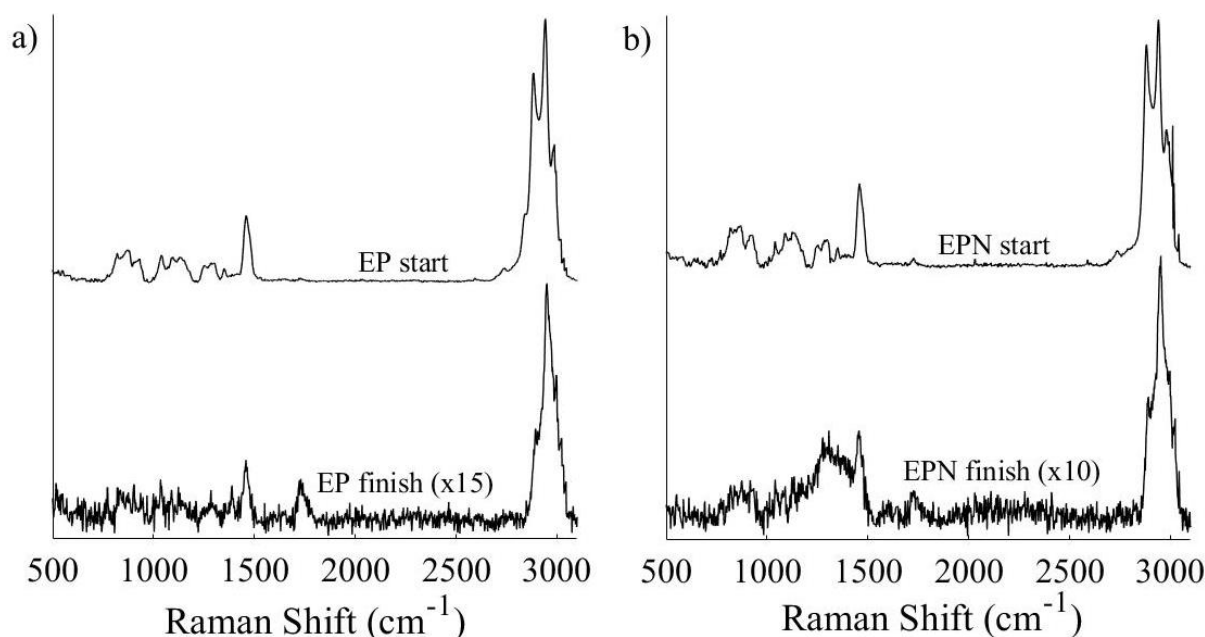


Figure 3: Offset Raman spectra for (a) EP and (b) EPN droplets. Top curves show the averaged first 10 scans, bottom curves show the averaged final 10 scans. Time between initial and final scans was ~250 min for EP and ~50 minutes for EPN. Note that to ease comparison the intensity of the final scans has been expanded 15-fold for EP and 10-fold for EPN. (600 groove, centred at 1900 cm⁻¹, 30 secs, 2 mW).

Considering the stability of the aerosol in the optical trap, it proved relatively facile to hold EP and monitor changes in the Raman spectra over time (analysis was conducted over a period in excess of 4 h). However, it is notable that an aerosol comprising ethanol alone, in the absence of P123, could only be contained in the trapping environment for less than a few seconds due to rapid evaporation. P123 therefore exerts a stabilising influence over the aerosol, significantly reducing evaporative losses of ethanol. Different physical mechanisms are discussed in order to explain this observation. The bulk solution employed has a concentration of P123 40 times larger (10 mM) than the reported critical micellisation concentration (CMC) of P123 of 0.25 mM.³⁰ Therefore, the P123 concentration within the aerosol is expected to be above the CMC and consequently it is suggested that micelle formation is reducing ethanol evaporation. Deconvolution of the C-H stretch region (2800-3025 cm⁻¹) of the Raman spectra provides

support for this hypothesis. The Raman band for each C-H stretch is blueshifted as a function of time (Table S1). Such behaviour has previously been shown to be associated with micelle formation in block copolymers and with the formation of structured networks in ethanol-water binary solutions.^{15,31} Further, the intensity of both the CH₃ symmetric and CH₃ asymmetric stretches increase relative to that of the CH₂ asymmetric stretch as a function of time (these ratios are denoted as I_2/I_1 and I_3/I_1 respectively in Table S1). This is indicative of a reduction in the mobility of CH₂ groups as a consequence of the increased structural rigidity of the extended micelle structure.³² Additionally, as a consequence of high surface:volume ratios with respect to the bulk solutions, surface effects may also play a role in stabilising the aerosol and reducing evaporative losses. For instance, Köhler theory suggests increased stability in water droplets containing salts and other dissolved compounds through a reduction in vapour pressure.³³ A similar process may take place in the aerosols in the present work whereby hygroscopic molecules dissolved in the droplets restrict the evaporation of ethanol through intermolecular interactions. Furthermore, P123 may preferentially segregate to the ethanol:air interface, with the hydrophilic head group on the ethanol side and the hydrophobic tail group on the air side.³⁴ This could lead to the creation of a surface film, thereby retarding evaporation of ethanol.

The relative stability of EP and EPN were investigated by monitoring changes in the relative intensity of the Raman peaks with time. The reduction in peak height relative to initial values for the 2928 cm⁻¹ C-H stretch and the 1454 cm⁻¹ bending vibration over time is shown in Figure 4.

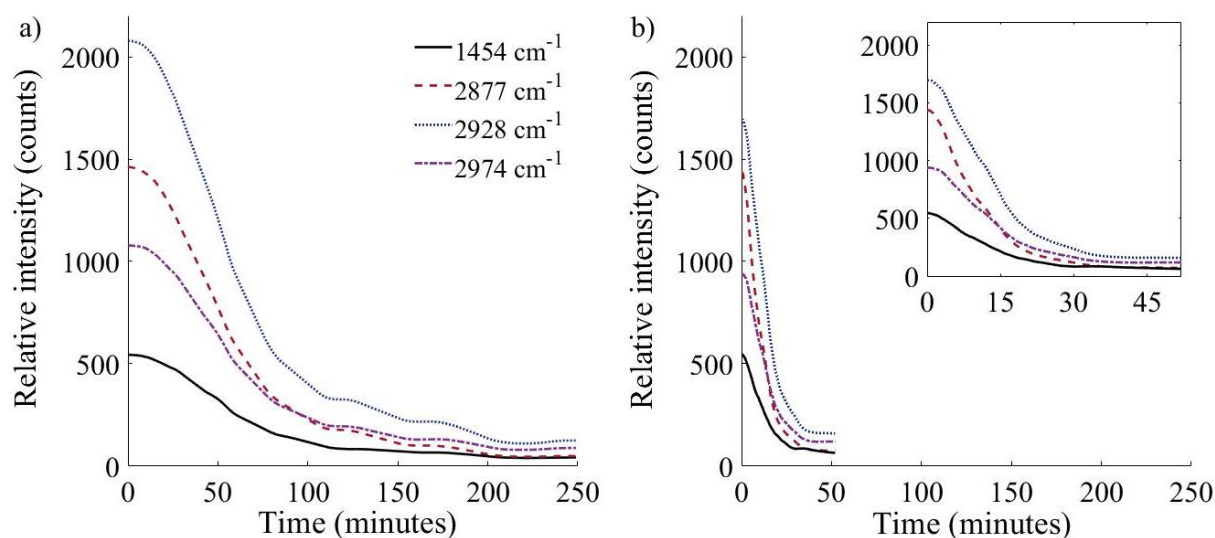


Figure 4: Change in Raman spectral intensity of C-H stretching and -CH_{2/3} bending peak for (a) EP and (b) EPN droplets with time (600 groove, centred at 1900 cm⁻¹, 30 secs, 2 mW).

The data show an initial induction period characterised by a relatively stable peak intensity, followed by a decrease in peak intensity which follows approximately exponential behaviour. The time at which the transition to exponential decay occurs has been identified from the derivative of the curves. For all aerosols, peak intensity data beyond this point were fitted to an exponential decay function of the form:

$$y = A_1 \times e^{\frac{-x}{t_1}} + y_0 \quad (1)$$

where y_0 = offset, A_1 = amplitude, t_1 = time constant, y = absorbance (counts), x = time (minutes). From this, the rates of decay ($1/t_1$) can be determined, thereby facilitating a comparison of the rate at which the same peaks in different droplets reduce in intensity. All exponential decay data have been tabulated in Table S2, and the fits to the original data are shown in Figures S4-S6.

EPN had a five times faster rate of decay relative to EP. Specifically, the CH₃/CH₂ bend at 1454 cm⁻¹ has decay rates of 0.075 min⁻¹ and 0.014 min⁻¹ for EPN and EP respectively. A similar relationship exists for the CH₃ symmetric stretch at 2928 cm⁻¹ which decays at 0.063 min⁻¹ and 0.015 min⁻¹ for EPN and EP respectively. This indicates a more rapid loss of ethanol from the aerosol in the case of EPN which can be directly correlated with the presence of HNO₃. It is proposed that HNO₃ destabilises the formation of micelles by P123, resulting in

a greater proportion of ‘free’ ethanol which rapidly evaporates. This is consistent with previous observations on the behaviour of pure ethanol where Fourier-transform infrared (FT-IR) spectroscopy investigations of bulk solutions showed that the addition of HCl to P123 impeded micellization.³⁵ The mechanism for this inhibition is attributed to increased hydrogen bonding between the solvent and P123 due the addition of the acidic proton. This observation supports the assumption that successful micelle formation restricts evaporation and thereby stabilises the droplet; in contrast impeding micelle formation accelerates evaporation and lowers the stability of the droplet.

3.2.2 Transformations in Metal-Containing Droplets

The inclusion of Al-iPr in EPNA and Ni(NO₃)₂·6H₂O in EPNAN, the latter aerosol comprising of all components of the synthesis mixture, has a clear impact on the spectrum of the aerosol (Figure 5). A new peak at 1048 cm⁻¹ appears in the spectra of both aerosols and is assigned to symmetric Al-NO₃ and Ni-NO₃ stretching vibrations.²³ The additional components also influence the stability of the aerosol within the optical trap. EPNA demonstrates high stability: an initial period of evaporation took place over the first 200 min, after which no further changes were observed in the spectra. During this initial evaporation period, a reduction in intensity with time of the peaks at 1454, 2877, 2928, and 2974 cm⁻¹ – all associated with ethanol (Table 1) – was observed. In contrast, a modest increase in peak intensity was observed for the band at 1048 cm⁻¹ (NO₃⁻ stretching). That this peak does not decrease in intensity implies that the Al-NO₃ species is not lost and therefore that either hydrolysis and condensation reactions occurred instantaneously or that they do not occur under these conditions in EPNA.

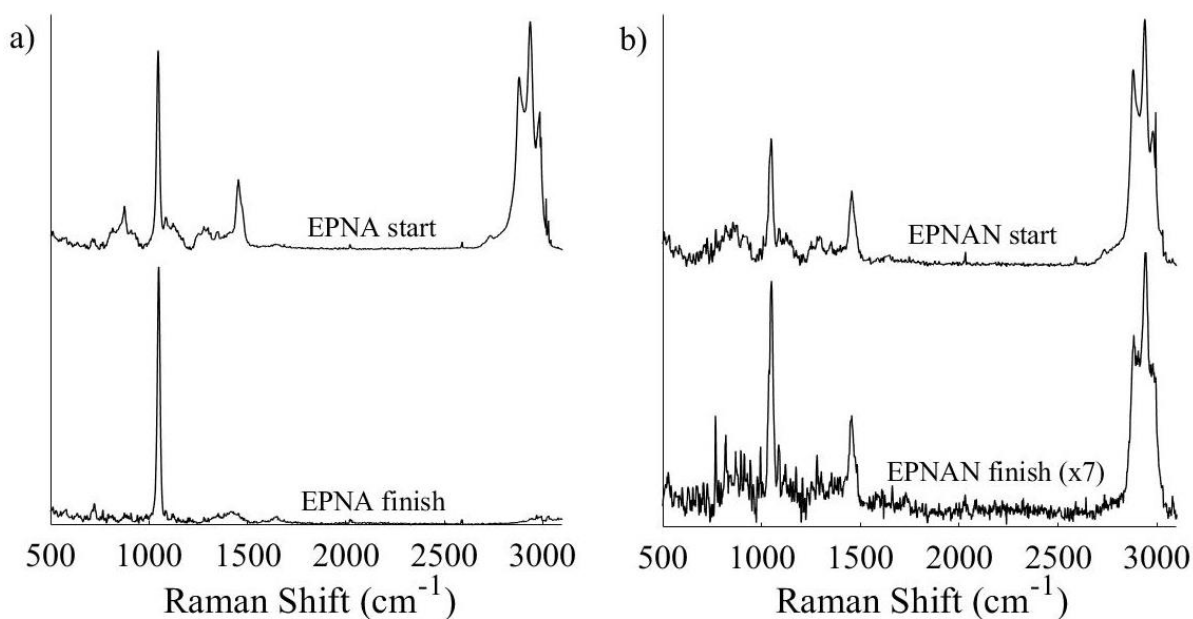


Figure 5: Offset Raman spectra for (a) EPNA and (b) EPNAN. Top curves show the averaged first 10 scans, bottom curves show the averaged final 10 scans. Time between initial and final scans was ~240 min for EPNA and ~50 minutes for EPNAN. Note that to ease comparison the intensity of the final scans for EPNAN (only) has been expanded 7-fold. (600 groove, centred at 1900 cm^{-1} , 30 secs, 2 mW).

Rates of decay of the bands at 1048, 1454 and 2928 cm^{-1} were calculated for EPNA and EPNAN in the same manner as for EP and EPN (Section 3.2.1). The variation in peak intensity with time for these vibrations is shown in Figure 6 and the exponential decay fits are shown in Figure S5. For EPNA the rates of decay of the ethanol C-H peaks at 1454 cm^{-1} and 2928 cm^{-1} are 0.012 and 0.015 min^{-1} respectively. This is a much slower rate of decay than observed for EPN where the corresponding values were 0.073 and 0.063 min^{-1} . The enhanced stability of EPNA with respect to EPN is suggestive of the formation of stable micelle-type structures, thereby limiting ethanol evaporation. Al-iPr may interact with the hydrophilic head groups of P123 creating a macro-structure; a similar process has previously been shown whereby micellisation is promoted through the addition of a low concentration of ethylammonium nitrate to block-copolymers.³⁰ In the present work the retardation of the loss of organic material prevents the aerosol changing in size either significantly or rapidly, thereby contributing to its longevity in the optical trap where it had the potential be held for a long period of time (hours).

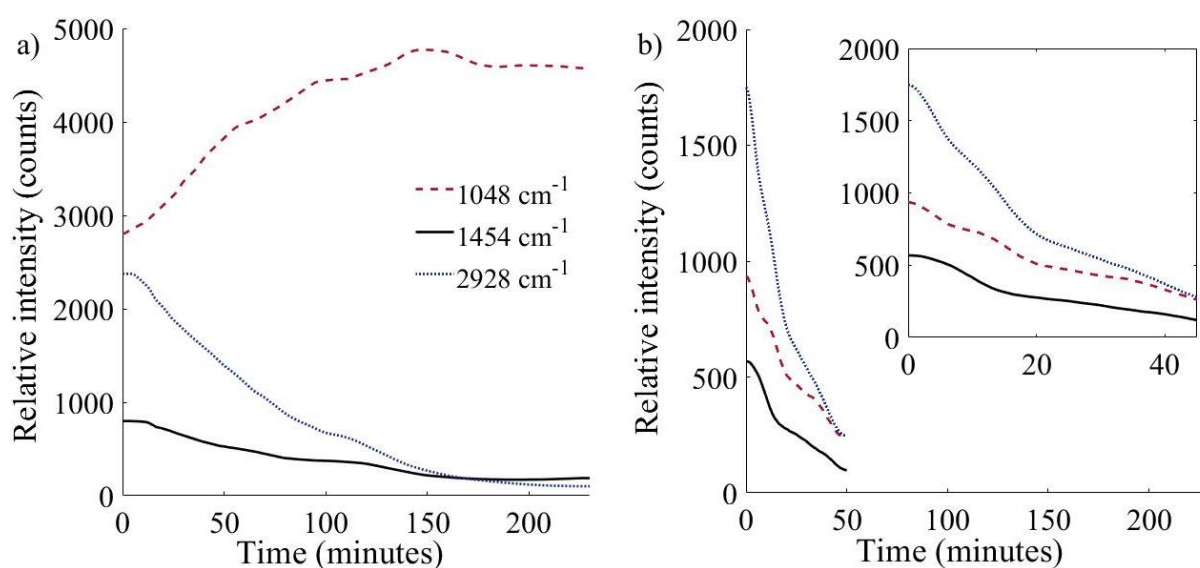


Figure 6: Raman absorbance of peaks at 1048, 1454 and 2928 cm^{-1} for (a) EPNA and (b) EPNAN fitted against time (600 groove, centred at 1900 cm^{-1} , 30 secs, 2 mW).

Upon addition of the final component, $\text{Ni}(\text{NO}_3)_2 \cdot 6\text{H}_2\text{O}$, no additional peaks were observed when compared to EPNA, although there are some differences when comparing the relative intensity of the peaks (Figure 5). Despite the similarity in the spectra, the behaviour of EPNAN differs from that of EPNA. While ethanol evaporates slightly more rapidly than for EPNA (decay rates of 0.035 and 0.044 min^{-1} for 1454 cm^{-1} and 2928 cm^{-1} in EPNAN as compared to 0.012 and 0.015 min^{-1} for EPNA) more dramatic differences are observed for the peak associated with Al- NO_3 and Ni- NO_3 stretch (1048 cm^{-1}). In EPNAN this peak also decreases rapidly over time with a rate of 0.029 min^{-1} . In contrast, in EPNA the peak at 1048 cm^{-1} peak increases from its initial intensity, attributed to an increase in Al- NO_3 bonds (Figure 6). The decrease in peak intensity observed in EPNAN indicates that $\text{Ni}(\text{NO}_3)_2 \cdot 6\text{H}_2\text{O}$ induces reactive chemical transformations in the system, either through hydrolysis and condensation reactions that are established to occur in bulk solutions (Section 1.0) or through an alternative reaction pathway (Section 3.4), with both scenarios ultimately resulting in the formation of cross-linked gel-phase. As with EP and EPN (Section 3.2.1), deconvolution of the C-H stretching region (Table S1) supports the conclusion that a more structured phase forms over time, with the intensity of the CH_3 symmetric and CH_3 asymmetric stretches relative to that of the CH_2 asymmetric stretch increasing over the analysis period.

Empirical observations of gelation in bulk solutions were conducted in order to inform analysis of the changes in Raman spectra with time recorded for the aerosols. Bulk EPNA and EPNAN

solutions with the same concentration as that nebulised in the *operando* studies were prepared. When kept in a sealed container over a period of >1 month, neither solution formed a gel, indicating that cross-linking reactions did not occur to a sufficient degree. However, both solutions successfully formed gels through passive evaporation, *i.e.* when stored in an open container without heating. The EPNAN bulk solution formed a gel after only ~30 minutes of evaporation; EPNA in contrast took over a week to form a gel. The EPNA gel formed over this period was notably less viscous than the EPNAN gel and could be poured (Figure S7). This behaviour is consistent with previous investigations on solutions of similar composition to EPNA where either times in excess of a week or enhanced evaporation at temperatures above 40 °C were required for gelation to occur.^{36–38} These observations confirm that a greater extent of reaction, induced by evaporation, occurs within the EPNAN solution when compared to the EPNA solution. Possible mechanistic pathways are discussed in detail in Section 3.4.

3.2.3 Droplet Size

In AASG synthesis, aerosol droplet size is directly correlated with the particle size of the final solid catalyst. Particle size can influence activity, selectivity, and stability.^{39,40} The size of particles constrained by optical tweezers, typically 0.01-10 μm , renders them unsuitable for size determination using imaging optics (for which they are too small) or using Rayleigh scattering calculations (for which they are too large).⁴¹ The presence of WGMs (Section 3.2) however allows the size of the trapped particles to be estimated using Mie theory. The high stability and strong Raman intensity exhibited by the EPNA droplet presents this as the optimal candidate for calculation of droplet size. The Mie scattering peak positions across the spectral range were compared to a theoretical model for Mie scattering assuming a homogeneous sphere and an initial refractive index approximating to the original components ($n = 1.430$). The initial radius of the droplet upon trapping was 1.32 μm . It then slowly reduced in size over the trapping period at a rate $\sim 0.15 \mu\text{m h}^{-1}$ to a radius of $0.96 \pm 0.1 \mu\text{m}$ whilst refractive index increased slightly to $n = 1.437$. This radius was maintained until the end of the trapping period beyond 200 min, at which point the aerosol is believed to comprise P123 an Al-NO₃ in a stabilised extended structure (Figure 7). The observed reduction in droplet size and increase in refractive index is ascribed to the evaporation of ethanol, based on the changes on the Raman spectra presented in Figure 6, where ethanol peaks at 1454 and 2928 cm^{-1} decreased before somewhat stabilising after 150 minutes.

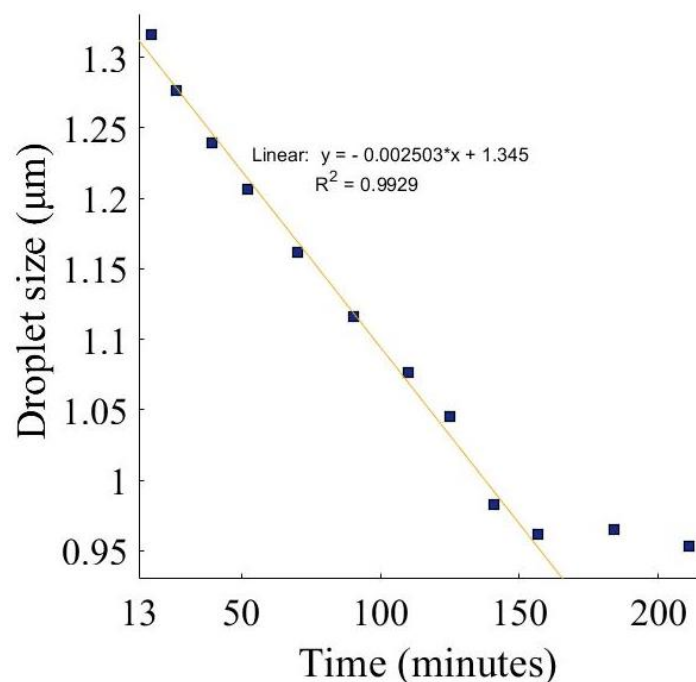


Figure 7: Droplet size in microns for EPNA against time in minutes.

3.3 Heated Aerosols

In order to gain further insights into reactions in the early stages of catalyst synthesis the influence of heating was examined, focusing on EPNA and EPNAN. These are denoted as HeEPNA and HeEPNAN; the He- prefix indicating heating. HeEPNAN contains all chemical components necessary for catalyst synthesis and is an accurate representation of the aerosols applied in AASG synthesis; HeEPNA contains all components bar $\text{Ni}(\text{NO}_3)_2 \cdot 6\text{H}_2\text{O}$ – the absence of which was observed to prevent reactions inducing cross-linking occurring at room temperature (Section 3.2). While some AASG syntheses apply temperatures of 100s °C, this study applies lower temperatures as the focus is on the initial reactions leading to formation of the gel. Furthermore, morphological changes in the droplet as it transitions from the liquid precursor to a solid gel intermediate and then to the final solid product mean that it would be experimentally challenging to retain the droplet in the optical trap during the latter stages of catalyst synthesis. The temperature at the droplet position was determined *via* calibration (Section 2.4).

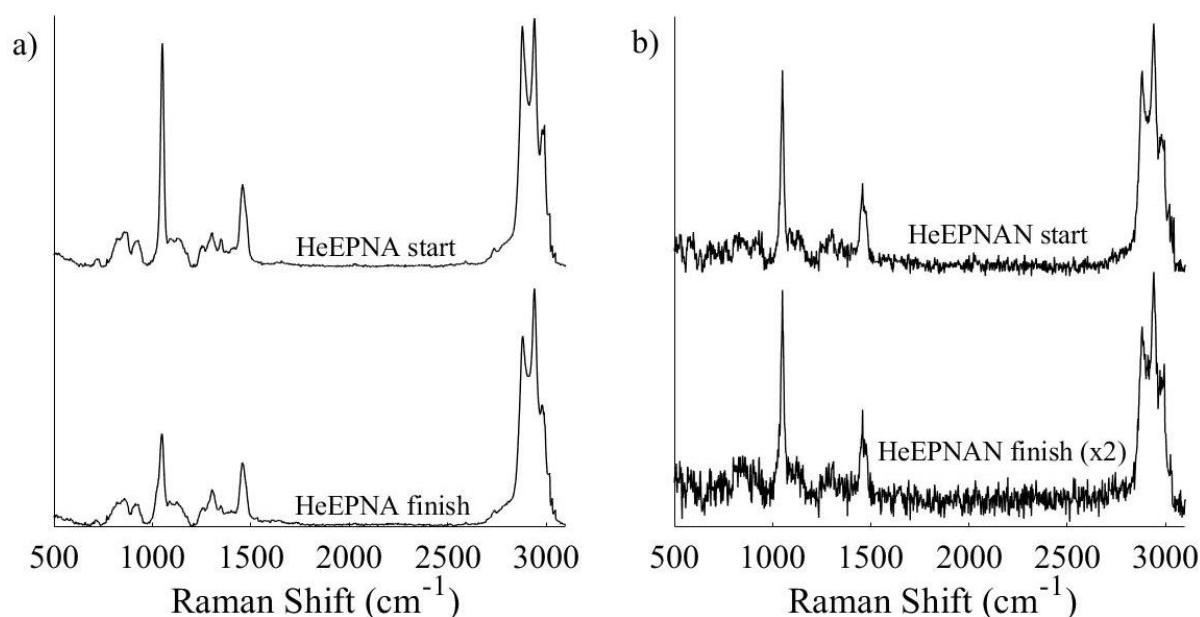


Figure 8: Offset Raman spectra for (a) HeEPNA and (b) HeEPNAN. Top curves show the averaged first 10 scans, bottom curves show the averaged final 10 scans. Time between initial and final scans was ~30 min for HeEPNA and ~15 minutes for HeEPNAN. Note that to ease comparison the intensity of the final scan for HeEPNAN been expanded 2-fold. (600 groove, centred at 1900 cm^{-1} , HeEPNA 30 sec, HeEPNAN 10 secs, 2 mW).

HeEPNA was heated to $120\text{ }^{\circ}\text{C}$ at $4\text{ }^{\circ}\text{C min}^{-1}$. Above this temperature the trapping of the aerosol became unstable. This instability can be caused by a combination of factors including decreasing aerosol mass, and changes in aerosol morphology and physical state. The initial (room temperature) and final ($120\text{ }^{\circ}\text{C}$) Raman spectra for HeEPNA are compared in Figure 8. Despite the elevated temperature, there is relatively little change in the spectra with time, the most significant change being a reduction in peak intensity of ~60% between the initial and final scans for the Al-NO_3 peak at 1048 cm^{-1} . This contrasts starkly with the room temperature behaviour of EPNA where: (i) the 1048 cm^{-1} stretch increased slightly over the 4 h period; and (ii) ethanol evaporation was inferred from the reduction in the 1454 & 2928 cm^{-1} peaks (Section 3.2). The rate of the decrease in intensity of the 1048 cm^{-1} peak increases significantly when the temperature exceeds $56\text{ }^{\circ}\text{C}$, as shown in Figure 9. After reaching this temperature the peak intensity falls by ~46% after 10 min, as compared to a decrease of only ~13% in the 10 min prior to reaching the temperature. This suggests that reactive transformations are initiated at ~ $56\text{ }^{\circ}\text{C}$ or above.

Counterintuitively, heating inhibits the evaporation of ethanol from the droplet as indicated by the stability of the bands arising from ethanol in the Raman spectra (1454 cm^{-1} CH_3 and CH_2

bend, 2877 cm^{-1} CH_2 symmetric stretch, 2928 cm^{-1} CH_3 symmetric stretch, and 2974 cm^{-1} CH_3 asymmetric stretch). A likely contributing factor to this phenomenon is the fact that the CMC of P123 decreases as temperature is increased. At $25\text{ }^\circ\text{C}$ the CMC of P123 is $0.03\text{ w/v}\%$; this decreases to $0.001\text{ w/v}\%$ at $35\text{ }^\circ\text{C}$.⁴² Therefore, even a relatively modest rise in temperature increases the strength and interconnectivity of the micelles formed by P123, thereby preventing evaporation of ethanol.⁴³ A second possible factor which may retard ethanol evaporation is that heating may induce an interaction between the precursors and the block copolymer P123 *via* an encapsulation-type mechanism.⁴⁴ This would inhibit evaporation of ethanol through the formation of a physical barrier around the droplet. The reduction in intensity over time of the peaks arising from components other than ethanol in HeEPNA suggests that the preliminary gelation reactions which occur in EPNA (Section 3.4) are initiated through the increase in the concentration of precursors in solution as a consequence of ethanol evaporation.

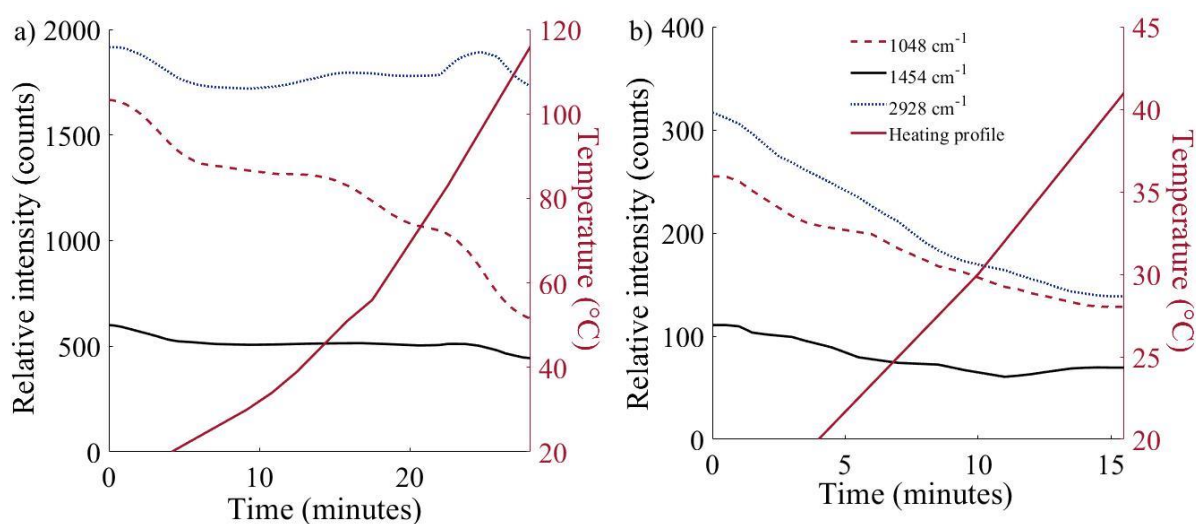


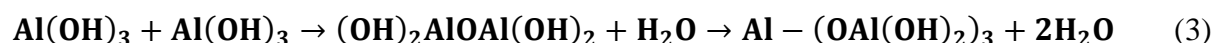
Figure 9: Raman spectral intensity of significant peaks for (a) HeEPNA and (b) HeEPNAN fitted against time with an additional temperature axis to display the temperature of the heated cell at that given point in time (600 groove, centred at 1900 cm^{-1} , HeEPNA 10 sec, HeEPNAN 30 sec, 2 mW).

HeEPNAN showed lower stability in the optical trap as compared to HeEPNA. This is consistent with room temperature studies (Section 3.2) where the same trend was observed when comparing EPNA and EPNAN. HeEPNAN was heated to $50\text{ }^\circ\text{C}$ at $1.5\text{ }^\circ\text{C min}^{-1}$, above which temperature it became unstable. Raman spectra at room temperature and $40\text{ }^\circ\text{C}$ are compared in Figure 8. Exponential decay analysis showed that all peaks decreased at a faster rate for HeEPNAN than EPNAN, although the extent of the increase varies for different peaks (Figure S6). The 2928 cm^{-1} CH_3 symmetric stretch exhibits decay rates of 0.074 min^{-1} and 0.044 min^{-1} in the heated and non-heated aerosols respectively, a relative increase of $\sim 50\%$. The

1454 cm⁻¹ CH₃/CH₂ bend, associated with both ethanol and P123, has an even greater proportionate increase in decay rate, from 0.035 min⁻¹ for EPNAN to 0.18 min⁻¹ for HeEPNAN (Figure S6). The higher rates of decay for the non-ethanol derived peaks suggests that the loss of peak intensity is not simply associated with increased evaporation but is instead indicative of increased reactivity and faster gelation upon the application of heating.

3.4 Mechanistic Insights

Previously proposed mechanisms for AASG syntheses involve hydrolysis and condensation reactions, similar to bulk syntheses.⁴⁵⁻⁴⁷ (Figure S1). Chemical equations for these processes are given in Equations 2 & 3. EPNA aerosol, which does not contain Ni, does not show evidence for hydrolysis and condensation reactions (Section 3.2.2). This is consistent with investigations on bulk samples where gelation only occurs at room temperature on long timescales (>1 week). In contrast, HeEPNA aerosol shows a reduction in the intensity of Al-NO₃ stretch (1048 cm⁻¹) over time during heating. This is indicative of chemical reactivity, and suggests that a necessary minimum activation energy is achieved upon heating. As previously stated in Section 3.2, the water content of each droplet is estimated at <4%; this is sufficiently low that no water spectral bands are observed in acquired Raman spectra. However, it has previously been observed that only a minimal amount of water is necessary to effect hydrolysis during bulk synthesis, with reaction occurring at an Al:P123:solvent:water molar ratio of 1:0.015:40.5:0.8.³⁶ The corresponding ratio in the present work is 0.47:0.012:19:1. It is therefore likely that there is sufficient water for hydrolysis reactions to proceed; this however only occurs upon the application of external heating. In contrast to aerosol EPNA and to bulk-phase systems, significant retardation of ethanol evaporation is observed for HeEPNA – postulated to be associated with enhanced micelle formation. These data therefore controvert the hypothesis that the reactive hydrolysis-polycondensation transformations that occur during synthesis (Section 1.0) are contingent on evaporation.



In contrast to EPNA, and similarly to HeEPNA, EPNAN shows evidence for chemical reactivity from the reduction in the Al-NO₃ and Ni-NO₃ associated stretch (1048 cm⁻¹). The additional component added to EPNA to form EPNAN is Ni(NO₃)₂·6H₂O. This increases the water content of the precursor mixture by 57%. It is possible that this additional water induces

hydrolysis, with the water molecules avoiding rapid evaporation in the aerosol due to their association to the nickel species. In this case water within the micelles would facilitate the processes shown in Figure S1.

A postulated alternative reaction mechanism is shown in Figure 10. An initial hydrolysis reaction (a) occurs forming aluminium hydroxide (Al-OH) as takes place in bulk solutions. This reaction requires water to proceed. Al-OH then reacts with HNO₃ (b) to form Al-NO₃ in solution. Elsewhere, this process is known from the dissolution of gibbsite (Al(OH)₃) in HNO₃.⁴⁸ This would therefore regenerate the water previously consumed in the hydrolysis reaction, allowing a cascade whereby further sequential hydrolysis (a) and neutralisation (b) reactions could occur. This mechanism is supported by the observation of increasing Al-NO₃ in EPNA over time. It is then proposed that there is insufficient energy available in the isothermal EPNA system to proceed with condensation reactions. When heat is applied, from observations of HeEPNA, sufficient energy is available to induce reactions forming Al-O-Al. For EPNAN however, the application of heat is not a prerequisite to induce reaction. A similar final transition to that occurring in HeEPNA is inferred to occur at room temperature in the presence of Ni; where an alternative pathway (c) of lower activation energy is available. This reaction involves rearrangement of the nickel nitrate aluminium complex to form a continuous Al-O-Ni-NO₃ structure, contrasting to the proposed Al-O-Al structure derived from HeEPNA.

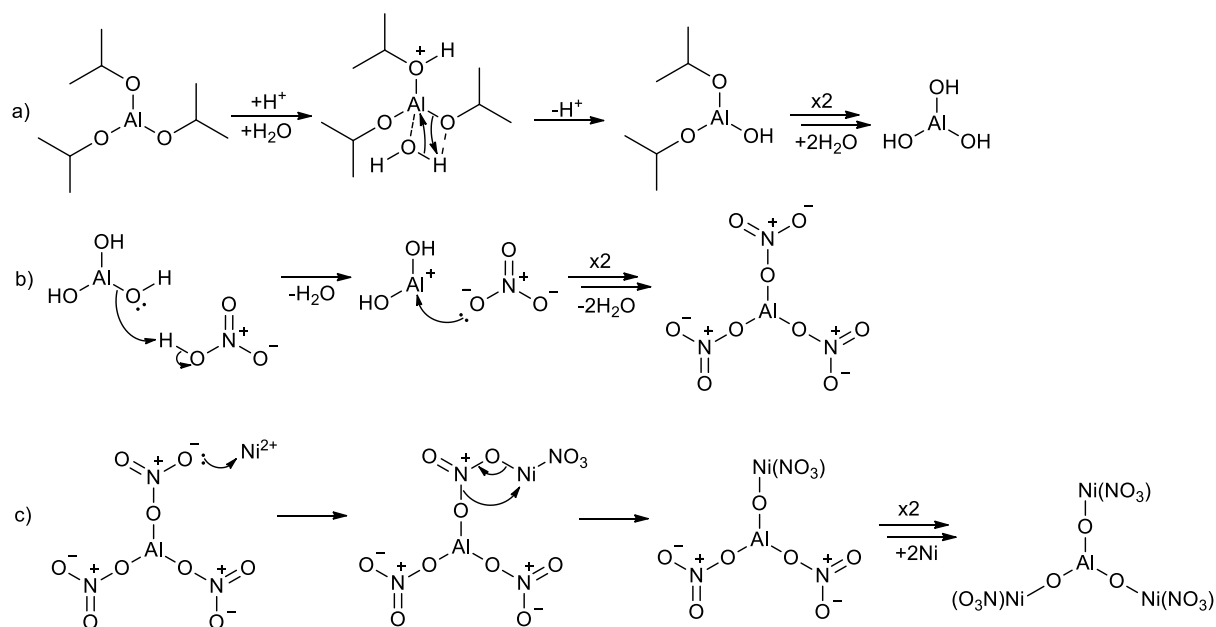
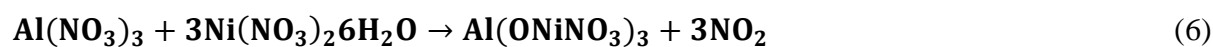


Figure 10: Postulated mechanism for the initial reactions in the AASG synthesis of Ni/Al₂O₃ based upon the Raman spectroscopy observations. Initial hydrolysis reaction of

Al-iPr (a), followed by neutralisation reaction between HNO₃ and Al-OH (b), and a final proposed cross linking (gelation) reaction caused by presence of the Ni²⁺ (c).

Changes in the stability of the aerosol within the optical trap upon the inclusion of Ni(NO₃)₂·6H₂O in the precursor solution are also indicative of chemical and physical transformations. In contrast to the exceptional stability of EPNA, EPNAN is held in the trap for only ~50 min. This relative instability is assigned to morphological changes induced by chemical reaction, specifically gelation within the aerosol resulting in changes to its size and shape. Figure 10 c) shows the postulated reaction mechanism leading to the formation of an extended aluminium nickel bonded complex within the aerosol, *i.e.* gelation (Equation 5). Spectroscopic support for this process comes from the reduction in intensity of aluminium nitrate (1048 cm⁻¹). This proposed reaction mechanism is consistent with previous studies of the bulk phase sol-gel synthesis of nickel aluminide (Ni₃Al) from Al-iPr, Ni(NO₃)₂, and HNO₃ in ethanol by Madon *et al.*⁴⁹ The balanced chemical equation for the proposed reaction pathway is therefore:



Which of these mechanisms, shown schematically in Figure S1 and Figure 10, is operating could be determined by synthesising the final Ni/Al₂O₃ catalysts in a flow tube reactor operating at high temperature using the same precursors described in Section 2.2. Full structural analysis of the final nanostructured catalyst using electron microscopy and X ray/neutron diffraction would elicit if the catalyst were highly ordered as Ni-Al-Ni-Al or exhibited structural and compositional heterogeneity, suggesting either the nickel induced reaction pathway or the condensation reaction observed in bulk solutions respectively.⁵⁰

4.0 Conclusions

Optical trapping combined with Raman spectroscopy has been demonstrated to be a successful approach to facilitate the interrogation of processes occurring during AASG catalyst synthesis. Droplets of ~1 μm in radius, based on analysis of EPNA, have been trapped and held for extended periods of up to 4 h depending on composition. The influence of each component within the Ni/Al₂O₃ precursor solution has been investigated. P123 stabilises the aerosol against ethanol evaporation, postulated to be a consequence of micelle formation, while HNO₃ acts to destabilise the formed micelles. The latter effect is overcome through the addition of Al-iPr, which is proposed to interact with the hydrophilic head groups of P123, thereby creating

a stable macro structure. No further transitions, such as gelation, are however inferred to occur at room temperature in the absence of nickel. Heating can however effect reactive transformations, seen to be initiated above ~ 56 °C. This is not accompanied by evaporation, hence suggesting a different mechanism than that reported from observations of bulk-phase systems. The addition of nickel induces reactivity at room temperature, with the rate of reaction enhanced upon heating. That reaction occurs even in the absence of external heating, suggests that a lower activation energy pathway exists in this system. Reaction mechanisms have been proposed for both routes which may result in final materials of differing long-range structure. The ability to successfully interrogate AASG syntheses spectroscopically during reaction can therefore bring new understanding to this emerging technology which can in turn support the design of improved processes and the synthesis of materials with specific targeted properties such as structure or morphology.

Supporting Information

Figure S1 – Mechanism for acid catalysed sol-gel formation

Figure S2 – Temperature calibration of heated cell

Figure S3 – Observed whispering gallery modes

Figure S4 – Exponential decay fitting for EP and EPN

Figure S5 – Exponential decay fitting for EPNA and EPNAN

Figure S6 – Exponential decay fitting for HeEPNA and HeEPNAN

Figure S7 – EPNA and EPNAN bulk observation

Table S1 – Extracted intensity and position of aliphatic (C-H) stretching

Table S2 – Tabulated exponential decay data

Acknowledgements

EPSRC is acknowledged for its support of the UK Catalysis Hub *via* grant EP/R026815/1; EPSRC is also thanked for funding a PhD studentship for GD *via* award EP/N509735/1. The Central Laser Facility (STFC) is acknowledged for providing access under grant App19130040. We also thank Olivia Ward for collecting the data in Figure S1 during her placement at the CLF. L. N. acknowledges the funding from the European Union's Horizon 2020 research and innovation programme under the Marie Skłodowska-Curie grant agreement No. 837794.

References

- (1) Debecker, D. P.; Le Bras, S.; Boissière, C.; Chaumonnot, A.; Sanchez, C. *Aerosol Processing: A Wind of Innovation in the Field of Advanced Heterogeneous Catalysts.*

- Chem. Soc. Rev.* **2018**, 47 (11), 4112–4155.
- (2) Innocenzi, P. Understanding Sol–Gel Transition through a Picture. A Short Tutorial. *J. Sol-Gel Sci. Technol.* **2020**, 544–550.
 - (3) Gonçalves, A. A. S.; Jaroniec, M. Evaporation-Induced Self-Assembly Synthesis of Nanostructured Alumina-Based Mixed Metal Oxides with Tailored Porosity. *J. Colloid Interface Sci.* **2019**, 537, 725–735.
 - (4) Peña Alvarez, M.; Mayorga Burrezo, P.; Iwamoto, T.; Qiu, L.; Kertesz, M.; Taravillo, M.; Baonza, V. G.; López Navarrete, J. T.; Yamago, S.; Casado, J.; et al. Ternary Oxide Nanostructured Materials for Supercapacitors: A Review. *Faraday Discuss.* **2014**, 4 (8), 1166–1169.
 - (5) Hua, M.; Zhang, S.; Pan, B.; Zhang, W.; Lv, L.; Zhang, Q. Heavy Metal Removal from Water / Wastewater by Nanosized Metal Oxides : A Review. **2012**, 212, 317–331.
 - (6) Liu, Q.; Gao, J.; Gu, F.; Lu, X.; Liu, Y.; Li, H.; Zhong, Z.; Liu, B.; Xu, G.; Su, F. One-Pot Synthesis of Ordered Mesoporous Ni-V-Al Catalysts for CO Methanation. *J. Catal.* **2015**, 326, 127–138.
 - (7) Pal, N.; Bhaumik, A. Ordered Mesoporous Ternary Mixed Oxide Materials as Potential Adsorbent of Biomolecules. *Chem. Phys. Lett.* **2012**, 535, 69–74.
 - (8) Vivian, A.; Soumoy, L.; Fusaro, L.; Fiorilli, S.; Debecker, D. P.; Aprile, C. Surface-Functionalized Mesoporous Gallosilicate Catalysts for the Efficient and Sustainable Upgrading of Glycerol to Solketal. *Green Chem.* **2021**, 23 (1), 354–366.
 - (9) Manangon-Perugachi, L. E.; Smeets, V.; Vivian, A.; Kainthla, I.; Eloy, P.; Aprile, C.; Debecker, D. P.; Gaigneaux, E. M. Mesoporous Methyl-Functionalized Titanosilicate Produced by Aerosol Process for the Catalytic Epoxidation of Olefins. *Catalysts* **2021**, 11 (2), 1–19.
 - (10) Meng, Q.; Liu, J.; Liu, L.; Xiong, G. Aerosol-Assisted Hydrothermal Synthesis of Hierarchical Sn-Beta Nanoaggregates in Fluoride Media. *Microporous Mesoporous Mater.* **2021**, 320 (March), 111090.
 - (11) Smeets, V.; Boissière, C.; Sanchez, C.; Gaigneaux, E. M.; Peeters, E.; Sels, B. F.; Dusselier, M.; Debecker, D. P. Aerosol Route to TiO₂-SiO₂ Catalysts with Tailored Pore Architecture and High Epoxidation Activity. *Chem. Mater.* **2019**, 31 (5), 1610–1619.
 - (12) Kim, A.; Sanchez, C.; Haye, B.; Boissière, C.; Sassoie, C.; Debecker, D. P. Mesoporous TiO₂ Support Materials for Ru-Based CO₂ Methanation Catalysts. *ACS Appl. Nano Mater.* **2019**, 2 (5), 3220–3230.

- (13) Haddrell, A. E.; Miles, R. E. H.; Bzdek, B. R.; Reid, J. P.; Hopkins, R. J.; Walker, J. S. Coalescence Sampling and Analysis of Aerosols Using Aerosol Optical Tweezers. *Anal. Chem.* **2017**, *89* (4), 2345–2352.
- (14) Ito, A.; Kamogawa, K.; Sakai, H.; Hamano, K.; Kondo, Y.; Yoshino, N.; Abe, M. Micelle Aggregating Condition of Fluorocarbon-Hydrocarbon Hybrid Surfactants in Aqueous Solution. *Langmuir* **1997**, *13* (11), 2935–2942.
- (15) Guo, C.; Wang, J.; Liu, H. Z.; Chen, J. Y. Hydration and Conformation of Temperature-Dependent Micellization of PEO-PPO-PEO Block Copolymers in Aqueous Solutions by FT-Raman. *Langmuir* **1999**, *15* (8), 2703–2708.
- (16) David G. Grier, N. A Revolution in Optical Manipulation. **2003**, *424* (August), 1–7.
- (17) Shepherd, R. H.; King, M. D.; Marks, A. A.; Brough, N.; Ward, A. D. Determination of the Refractive Index of Insoluble Organic Extracts from Atmospheric Aerosol over the Visible Wavelength Range Using Optical Tweezers. *Atmos. Chem. Phys.* **2018**, *18* (8), 5235–5252.
- (18) Hunt, O. R.; Ward, A. D.; King, M. D. Laser Heating of Sulfuric Acid Droplets Held in Air by Laser Raman Tweezers. *RSC Adv.* **2013**, *3* (42), 19448–19454.
- (19) Boyer, H. C.; Gorkowski, K.; Sullivan, R. C. In Situ PH Measurements of Individual Levitated Microdroplets Using Aerosol Optical Tweezers. *Anal. Chem.* **2020**, *92* (1), 1089–1096.
- (20) McGrory, M. R.; King, M. D.; Ward, A. D. Using Mie Scattering to Determine the Wavelength-Dependent Refractive Index of Polystyrene Beads with Changing Temperature. *J. Phys. Chem. A* **2020**, *124* (46), 9617–9625.
- (21) Aminzadeh, A.; Sarikhani-fard, H. Raman Spectroscopic Study of Ni/Al₂O₃ Catalyst. *Spectrochim. Acta - Part A Mol. Biomol. Spectrosc.* **1999**, *55* (7–8), 1421–1425.
- (22) Burikov, S.; Dolenko, T.; Patsaeva, S.; Starokurov, Y.; Yuzhakov, V. Raman and IR Spectroscopy Research on Hydrogen Bonding in Water-Ethanol Systems. *Mol. Phys.* **2010**, *108* (18), 2427–2436.
- (23) Carter, J. C.; Khulbe, P. K.; Gray, J.; Van Zee, J. W.; Angel, S. M. Raman Spectroscopic Evidence Supporting the Existence of Ni⁴(OH)₄⁴⁺ in Aqueous, Ni(NO₃)₂ Solutions. *Anal. Chim. Acta* **2004**, *514* (2), 241–245.
- (24) McLaughlin, R. P.; Bird, B.; Reid, P. J. Vibrational Analysis of Isopropyl Nitrate and Isobutyl Nitrate. *Spectrochim. Acta - Part A Mol. Biomol. Spectrosc.* **2002**, *58* (12), 2571–2580.
- (25) Ruan, H. D.; Frost, R. L.; Kloprogge, J. T. Comparison of Raman Spectra in

- Characterizing Gibbsite, Bayerite, Diaspore and Boehmite. *J. Raman Spectrosc.* **2001**, *32* (9), 745–750.
- (26) Dantham, V. R.; Bisht, P. B.; Dobal, P. S. Whispering Gallery Modes and Effect of Coating on Raman Spectra of Single Microspheres. *J. Raman Spectrosc.* **2011**, *42* (6), 1373–1378.
- (27) Hopkins, R. J.; Mitchem, L.; Ward, A. D.; Reid, J. P. Control and Characterisation of a Single Aerosol Droplet in a Single-Beam Gradient-Force Optical Trap. *Phys. Chem. Chem. Phys.* **2004**, *6* (21), 4924–4927.
- (28) Kolwas, M.; Jakubczyk, D.; Derkachov, G.; Kolwas, K. Interaction of Optical Whispering Gallery Modes with the Surface Layer of Evaporating Droplet of Suspension. *J. Quant. Spectrosc. Radiat. Transf.* **2013**, *131*, 138–145.
- (29) Li, R.; D’Agostino, C.; McGregor, J.; Mantle, M. D.; Zeitler, J. A.; Gladden, L. F. Mesoscopic Structuring and Dynamics of Alcohol/Water Solutions Probed by Terahertz Time-Domain Spectroscopy and Pulsed Field Gradient Nuclear Magnetic Resonance. *J. Phys. Chem. B* **2014**, *118* (34), 10156–10166.
- (30) He, Z.; Alexandridis, P. Micellization Thermodynamics of Pluronic P123 (EO20PO70EO20) Amphiphilic Block Copolymer in Aqueous Ethylammonium Nitrate (EAN) Solutions. *Polymers (Basel)*. **2017**, *10* (1).
- (31) Li, F.; Men, Z.; Li, S.; Wang, S.; Li, Z.; Sun, C. Study of Hydrogen Bonding in Ethanol-Water Binary Solutions by Raman Spectroscopy. *Spectrochim. Acta - Part A Mol. Biomol. Spectrosc.* **2018**, *189*, 621–624.
- (32) da Costa, A. M. A.; Geraldés, C. F. G. C.; Teixeira-Dias, J. J. C. Micellar Aggregation of CTAB in Water and Chloroform Solutions—a Study by Laser Raman Spectroscopy. *J. Colloid Interface Sci.* **1982**, *86* (1), 254–259.
- (33) Ferron, G. A.; Soderholm, S. C. Estimation of the Times for Evaporation of Pure Water Droplets and for Stabilization of Salt Solution Particles. *J. Aerosol Sci.* **1990**, *21* (3), 415–429.
- (34) Shao, X.; Duan, F.; Hou, Y.; Zhong, X. Role of Surfactant in Controlling the Deposition Pattern of a Particle-Laden Droplet: Fundamentals and Strategies. *Adv. Colloid Interface Sci.* **2020**, *275*, 102049.
- (35) Yang, B.; Guo, C.; Chen, S.; Junhe, M.; Wang, J.; Liang, X.; Zheng, L.; Liu, H. Effect of Acid on the Aggregation of Poly(Ethylene Oxide)-Poly(Propylene Oxide)-Poly(Ethylene Oxide) Block Copolymers. *J. Phys. Chem. B* **2006**, *110* (46), 23068–23074.

- (36) Moatti, A.; Javadpour, J.; Anbia, M.; Badiei, A. The Correlation between Aging Time and Pore Characteristics in the Synthesis of Mesoporous Al₂O₃. *Ceram. Int.* **2014**, *40* (7), 10231–10236.
- (37) Singh, P.; Maiti, P. K.; Sen, K. Pristine and Modified-Mesoporous Alumina : Molecular Assistance-Based Drug Loading and Sustained Release Activity. *Bull. Mater. Sci.* **2020**, *43* (1), 1–9.
- (38) Niesz, K.; Yang, P.; Somorjai, G. A. Sol-Gel Synthesis of Ordered Mesoporous Alumina. **2005**, 1986–1987.
- (39) Harju, H.; Pipitone, G.; Lefferts, L. Influence of the Catalyst Particle Size on the Aqueous Phase Reforming of N-Butanol Over Rh/ZrO₂. *Front. Chem.* **2020**, *8* (January), 1–13.
- (40) Wang, H.; Lu, J. A Review on Particle Size Effect in Metal-Catalyzed Heterogeneous Reactions. *Chinese J. Chem.* **2020**, *38* (11), 1422–1444.
- (41) Nieminen, T. A.; Loke, V. L. Y.; Stilgoe, A. B.; Knöner, G.; Brańczyk, A. M.; Heckenberg, N. R.; Rubinsztein-Dunlop, H. Optical Tweezers Computational Toolbox. *J. Opt. A Pure Appl. Opt.* **2007**, *9* (8).
- (42) Bodratti, A. M.; Alexandridis, P. Formulation of Poloxamers for Drug Delivery. *J. Funct. Biomater.* **2018**, *9* (1).
- (43) Ashraf, U.; Chat, O. A.; Maswal, M.; Jabeen, S.; Dar, A. A. An Investigation of Pluronic P123-Sodium Cholate Mixed System: Micellization, Gelation and Encapsulation Behavior. *RSC Adv.* **2015**, *5* (102), 83608–83618.
- (44) Sakai-Kato, K.; Nishiyama, N.; Kozaki, M.; Nakanishi, T.; Matsuda, Y.; Hirano, M.; Hanada, H.; Hisada, S.; Onodera, H.; Harashima, H.; et al. General Considerations Regarding the in Vitro and in Vivo Properties of Block Copolymer Micelle Products and Their Evaluation. *J. Control. Release* **2015**, *210*, 76–83.
- (45) Marage, P.; Langlet, M.; Joubert, J. C. Understanding and Improving the Deposition Conditions of SiO₂ Thin Films Obtained by Ultrasonic Sol-Gel Procedure - Code: EP30. *J. Sol-Gel Sci. Technol.* **1994**, *2* (1–3), 615–618.
- (46) Langlet, M.; Walz, D.; Marage, P.; Joubert, J. C. Glass and Ceramic Thin Films Deposited by an Ultrasonically Assisted Sol-Gel Technique. *Thin Solid Films* **1992**, *221* (1–2), 44–54.
- (47) Primeau, N.; Vautey, C.; Langlet, M. The Effect of Thermal Annealing on Aerosol-Gel Deposited SiO₂ Films: A FTIR Deconvolution Study. *Thin Solid Films* **1997**, *310* (1–2), 47–56.

- (48) Dietzel, M.; Böhme, G. The Dissolution Rates of Gibbsite in the Presence of Chloride, Nitrate, Silica, Sulfate, and Citrate in Open and Closed Systems at 20°C. *Geochim. Cosmochim. Acta* **2005**, *69* (5), 1199–1211.
- (49) Madon, R. H.; Fawzi, M.; Sarwani, K. I.; Osman, S. A.; Razali, M. A.; Mohammad, A. W. Effect of Reaction Temperature on Steam Methane Reforming's Yield over Coated Nickel Aluminide (Ni₃Al) Catalyst in Micro Reactor. *J. Adv. Res. Fluid Mech. Therm. Sci.* **2018**, *50* (2), 170–177.
- (50) Baerlocher, C.; Gramm, F.; Massüger, L.; McCusker, L. B.; He, Z.; Hövöller, S.; Zou, X. Structure of the Polycrystalline Zeolite Catalyst IM-5 Solved by Enhanced Charge Flipping. *Science* (80-.). **2007**, *315* (5815), 1113–1116.

Table of Contents (TOC) Graphic

